Gunn, A., Rubanenko, L., and Lapôtre, M.G.A., 2022, Accumulation of windblown sand in impact craters on Mars: Geology, v. 50, https://doi.org/10.1130/G49936.1

Supplemental Material for "Accumulation of windblown sand in impact craters on Mars."

Andrew Gunn[1,2,*], Lior Rubanenko[2], and Mathieu G. A. Lapôtre[2]

[1]*School of Earth, Atmosphere & Environment, Monash University, Clayton, VIC 3800, Australia*

[2]*Geological Sciences, Stanford University, Stanford, CA 94305, USA*

[*]*Corresponding Author: a.gunn@monash.edu*

INTRACRATER EOLIAN DEPOSIT VOLUME CALCULATION

We calculate deposit volume in a crater as the product of the dune-field area and its average thickness. Dune-field areas are calculated from the mapped polygons of Hayward et al. (2007, 2010, 2012) and Fenton (2020). These polygons were traced in longitude-latitude coordinates using JMARS; we projected the mapped boundaries onto an oblique cylindrical equal-area cartesian map centered on the dune-field center-point. The average thickness of the dune-field deposit was defined as the average of the deposit thickness estimated at every grid point of the Mars Orbiter Laser Altimeter (MOLA; Zuber et al., 1992) topographic data contained within the dune-field boundary. Before evaluating the thickness in each grid point, the MOLA topographic data, dune-field boundary, and crater boundary were all projected onto the same oblique cylindrical equal-area cartesian map centered on the crater center-point. Crater boundaries and centers were extracted from the dataset of Robbins & Hynek (2012). Center points were provided as longitude-latitude coordinates and crater boundary was traced assuming a circular rim of radius half the diameter value provided by Robbins & Hynek (2012). The most up-to-date version (August 30th 2014) of the Robbins & Hynek (2012) crater dataset was used.

The following algorithm was implemented to determine deposit thickness in each MOLA grid point (also illustrated in Fig. 1B&C). First, a circle concentric to the crater rim and that intersects with the target grid point (Point A) was drawn. Second, the closest MOLA grid points (Points B and C) to the intersections between the circle and the dune-field polygon edge were found. A linear interpolation of elevation along the arc of the circle between Points B and C was made to approximate crater-floor topography below the dune field, and evaluated at Point A. This value was assumed to be the elevation of the crater floor below the eolian deposit in A. Finally, the deposit thickness in Point A was calculated by subtracting the estimated basement elevation to the MOLA elevation in Point A. This process was repeated in all MOLA grid points contained within the mapped dune field, allowing us to calculate an average deposit thickness.

In instances where parts of a dune field had lower MOLA surface elevations than the interpolated basement elevation, we assumed that the dune field thickness there was zero. Furthermore, 1.3% of mapped dune fields do not inscribe a single MOLA grid point and were thus not included in the analysis; 3.1% of mapped dune fields yielded zero deposit thickness where dunes had been mapped and were thus not included in the analysis. Some mapped dune fields cover the crater center, a configuration that leads to the existence of MOLA grid points contained within the dune field for which the intersecting circle does not intersect with the dune-field boundary; for these points, we assume that the basement elevation was the same as the elevation observed at the dune-field edge closest to the crater center.

Our algorithm would only provide a “perfect” estimation of deposit volume if the crater was perfectly radially symmetric and the dune field within it did not overlay the crater center.

Because most craters have relatively flat floors, dune fields overlaying crater centers are not likely to be a large source of error. Furthermore, most craters are approximately radially symmetric, such that the assumption of radial symmetry is reasonable. The linear interpolation, topographic data, mapping of dune field boundaries, and projections also introduce small errors; however, these errors are not expected to be systematic, and given the large number of datapoints, should cancel out in a "central-limit theorem" sense.

To verify the robustness of our whole-deposit volume estimates using MOLA topography, we compared them to the volumes of intracrater barchan dunes mapped by Rubanenko et al. (in review). Rubanenko et al. (in review) used a convolutional neural network to outline individual barchan dunes globally and achieved a >75% detection rate. For each crater that contains detected barchans, we computed the total volume of the barchan dunes as the sum of the product of their planform surface area to their heights (as estimated from the length of dune slipfaces; Bourke et al., 2009). If our MOLA estimates are indeed representative of true volumes of windblow sediments, we expect to find a strong correlation between them and the sum of the volumes of individual barchan dunes, with the latter being possibly orders of magnitude smaller than the former because it solely includes barchan dunes (no other dune types or surrounding sand sheets), and not all barchan dunes were detected. We find that our MOLA estimates of whole-deposit volumes are indeed highly correlated ($R^2 = 0.39, p < 0.01$) with the measured sum of detected barchan volumes within the same crater, confirming that these deposits are primarily composed of windblown dune-forming sand and that our inferred relative trends in sand volumes are robust (Fig. S5).

LITHOLOGY ERODIBILITY CALCULATION

We used the geologic map of Tanaka et al. (2014) to identify units of known age (as previously estimated from crater chronology) and lithology on Mars. Each unit in the map belongs to one of 44 unique unit types, each of which is associated with one of 26 sub-lithologies and span one or more of Mars' 8 geologic epochs. The 26 sub-lithologies belong to 8 lithology groups. Because the oldest age of a given unit is the start of the epoch during which it formed, we were able to place a lower bound on the accumulation rate of sediments in a given unit. We therefore assigned a maximum age (one of 8 values) and a lithologic type (one of 8 values) to all impact craters >1 km in diameter that contain dune fields. The age values for the epoch boundaries provided by Tanaka et al. (2014) and were determined using crater counting techniques.

To assign a relative erodibility to each lithologic type, we exploited the fact that there are units of equal age but different lithologies for which we could compare accumulation thicknesses. To that end, we first needed to appropriately normalize the thicknesses by unit, crater, and dune-field areas. An implicit assumption in this approach is that these units experienced a similar erosive forcing (i.e., a similar climate history). Whereas this assumption may not be valid everywhere or at all times in Mars' history, potential spatial biases are largely mitigated by the fact that most lithologies extend across a wide range in latitude. Another implicit assumption in this method is that the eolian sand deposited in craters was largely eroded from the unit the crater is in, and that the area over which this erosion takes place scales with the size of the crater. The analysis of erosion process presented in the main text shows that local processes likely dominate sand supply of intracrater dune fields, supporting that the latter assumption is reasonable.

Our workflow to determine the relative erodibility of all lithologic types is illustrated in Figure S1. First, equivalent deposit thicknesses were assigned to each epoch-lithology pairing (Fig. S1A). For each unit associated with that epoch-lithology pair, we calculated an equivalent deposit thickness by dividing the sum volume of intracrater eolian deposits in all large (upper-quartile in size) craters within that unit by the sum area of those craters (including the large craters than do not contain deposits). We then calculated the average equivalent deposit thickness for that epoch-lithology pair using a unit-area weighted mean of the equivalent deposit thicknesses for the units that belong to the pairing. Second, we calculated the ratio of equivalent deposit thicknesses of epoch-lithology pairs for lithology pairs from the same epoch, and assigned a relative equivalent deposit thickness to each lithology pair by taking the average of all available ratios of equivalent deposit thicknesses (Fig. S1A&B). A high value for this ratio implies that the numerator lithology is more erodible than the denominator lithology (row more erodible than column in Fig. S1B). An example of this calculation is given for the erodibility of basin units relative to volcanic units in Figure S1A&B: it is the average ratio of the area-corrected thicknesses for basins (green dots in Fig. S1A) to volcanics (blue dots in Fig. S1A) across shared ages. Third, the erodibility of each lithologic type was defined as a geometric mean of all ratios of equivalent deposit thicknesses, where the lithology of interest appears on the numerator and the denominator is a different lithology. An example of this calculation is given for the erodibility of polar units in Figure S1B&C: the geometric mean (black line in Fig. S1C) of the pairings where polar lithology is the numerator (yellow-crossed in Fig. S1B) and the reciprocal of the pairings where it is the numerator (purple-crossed in Fig. S1B).

Several approaches were used to manage the sparsity of data in this process. First, some possible lithology-age pairings are not represented by any mapped unit on Mars (e.g., no Early

Noachian polar unit was identified by Tanaka et al., 2014), and some mapped units do not contain any > 1 km crater centers in the Robbins & Hynek (2012) dataset. Such "missing data" (empty white elements in Fig. S1A) prevented a comparison of some lithologic types, for a given epoch. Second, certain lithology-epoch pairings did not contain any units with eolian deposits in large craters (black-dotted white elements in Fig. S1A); a relative accumulation thickness between these pairings and others of equal age could thus not be directly determined. When averaging relative equivalent deposit thicknesses for a given age, such undefined- or zero-sized deposit thicknesses were not included. Notably, there are no units of the "apron" lithologic type which could be compared to other units (entire bottom row of Fig. S1A is empty). Third, there are lithology pairings for which there are no units of equal age with defined thicknesses (black-dotted elements in Fig. S1B); relative thicknesses could still be determined for these pairings through a chain-rule calculation involving a mutual third lithologic type – to find the relative thicknesses of lithologies A and B, which do not contain units of common age, we find the average of the product of relative thickness of lithology A to lithology C and lithology C to lithology B, where lithology C must contain units of common age with units within lithology A and units within lithology B. Algorithmically, the chain-rule approach was performed after the calculation of relative equivalent deposit thicknesses and before relative erodibility.

SADLER EFFECT AND APPARENT ACCUMULATION RATES

Apparent accumulation rates of deposited sediments, measured as deposit thickness divided by duration since the onset of deposition, are biased in space and time relative to instantaneous or short-term accumulation rates (Sadler, 1981) – a phenomenon known as the Sadler effect. A spatial bias arises from the fact that accumulation rates are typically only calculated or available where deposits have been preserved, therefore underestimating erosion and increasing the apparent accumulation rate relative to true net accumulation rates. A temporal bias arises from the fact that as one calculates accumulation rates over longer periods of time, the more and longer episodes of zero accumulation or erosion are included within the averaging timespan as the probability distribution of wait times between deposition events is heavy-tailed (Schumer & Jerolmack, 2009). The temporal Sadler effect implies that, when comparing apparent accumulation rates that were calculated over different durations before present, the younger apparent rate will be closer to short-term deposition rates than the older apparent rate; this effect breaks down when the two apparent rates are averaged over timescales that are longer than the longest period of inactivity one could possibly expect between depositional or erosional events (Schumer & Jerolmack, 2009).

The accumulation rates calculated in this study (Fig. 4B) are not subject to the spatial bias but they are subject to the temporal bias. The spatial bias is accounted for by averaging accumulation rates for a given unit across all large (upper-quartile by size) craters within that unit, inclusive of those that do not contain mapped eolian deposits. As the intermittency of erosion and deposition events cannot reasonably exceed 1 billion years, a temporal bias only exists when comparing Mid-to-Late Amazonian accumulation rates to older accumulation rates; but not when comparing rates between epochs in the Early Amazonian and older: this is because it appears unreasonable that erosion of these units could have ceased for longer periods than 1 billion years.

When we view the data in this study such that it is subject to the spatial bias, by only looking at the deposit thickness (and not normalizing by crater area) accumulation rates over time, we can compare it 'apples-to-apples' with other published data subject to the same bias

(Fig. S4). The observed thicknesses provide apparent accumulation rates which are consistent with other observations from Mars (Golombek et al., 2014). Moreover, when compared to similarly biased data from Earth (Sadler & Jerolmack, 2015), we see that martian sediment accumulation rates are around two orders of magnitude slower than on Earth (Fig. S4), which is consistent with the expectation that the erosivity of Earth's active planet-wide hydrological cycle is far higher than Mars' dry and thin modern atmosphere.

REFERENCES CITED

Bourke, M.C., Balme, M., Beyer, R.A., Williams, K.K. and Zimbelman, J., 2006, A comparison of methods used to estimate the height of sand dunes on Mars: Geomorphology, 81(3-4), pp.440-452.

Fenton, L.K., 2020, Updating the global inventory of dune fields on Mars and identification of many small dune fields: Icarus, 352, p.114018.

Golombek, M.P., Warner, N.H., Ganti, V., Lamb, M.P., Parker, T.J., Fergason, R.L. and Sullivan, R., 2014, Small crater modification on Meridiani Planum and implications for erosion rates and climate change on Mars: Journal of Geophysical Research: Planets, 119(12), pp.2522-2547.

Hayward, R.K., Mullins, F.K., Fenton, L.K., Hare, T.M., Titus, T.N., Bourke, M.C., Colaprete, A., and Christensen, P.R., 2007, Mars global digital dune database: MC-2 – MC-29: US Geological Survey Open-File report 2007-1158.

Hayward, R.K., Fenton, L.K., Tanaka, K.L., Titus, T.N., Colaprete, A., and Christensen, P.R., 2010, Mars global digital dune database: MC-1: US Geological Survey Open-File Report 2010-1170.

Hayward, R.K., Fenton, L.K., Titus, T.N., Colaprete, A., and Christensen, P.R., 2012, Mars global digital dune database: MC-30: US Geological Survey Open-File Report 2012-1259.

Piqueux, S., Buz, J., Edwards, C.S., Bandfield, J.L., Kleinböhl, A., Kass, D.M., Hayne, P.O., MCS and THEMIS Teams, 2019, Widespread shallow water ice on Mars at high latitudes and mid latitudes: Geophysical Research Letters, 46(24), pp.14290-14298.

Robbins, S.J. and Hynek, B.M., 2012, A new global database of Mars impact craters ≥ 1 km: 1. Database creation, properties, and parameters: Journal of Geophysical Research: Planets, 117(E5).

Sadler, P.M., 1981, Sediment accumulation rates and the completeness of stratigraphic sections: The Journal of Geology, 89(5), pp.569-584.

Sadler, P.M. and Jerolmack, D.J., 2015, Scaling laws for aggradation, denudation and progradation rates: the case for time-scale invariance at sediment sources and sinks: Geological Society, London, Special Publications, 404(1), pp.69-88.

Schumer, R. and Jerolmack, D.J., 2009, Real and apparent changes in sediment deposition rates through time: Journal of Geophysical Research: Earth Surface, 114(F3).

Tanaka, K.L., Skinner Jr, J.A., Dohm, J.M., Irwin III, R.P., Kolb, E.J., Fortezzo, C.M., Platz, T., Michael, G.G., and Hare, T.M., 2014, Geologic map of Mars., US Geological Survey Scientific Investigations Map 2014-3292.

Rubanenko, L., Gunn, A., Fenton, L.K, Ewing, R.C., Lapôtre, M.G.A., 2021, Global morphometrics of barchan dunes on Mars revealed by an artificial neural network (in review).

Zuber, M.T., Smith, D., Solomon, S.C., Muhleman, D.O., Head, J.W., Garvin, J.B., Abshire, J.B. and Bufton, J.L., 1992, The Mars Observer laser altimeter investigation: Journal of Geophysical Research: Planets, 97(E5), pp.7781-7797.

FIGURES

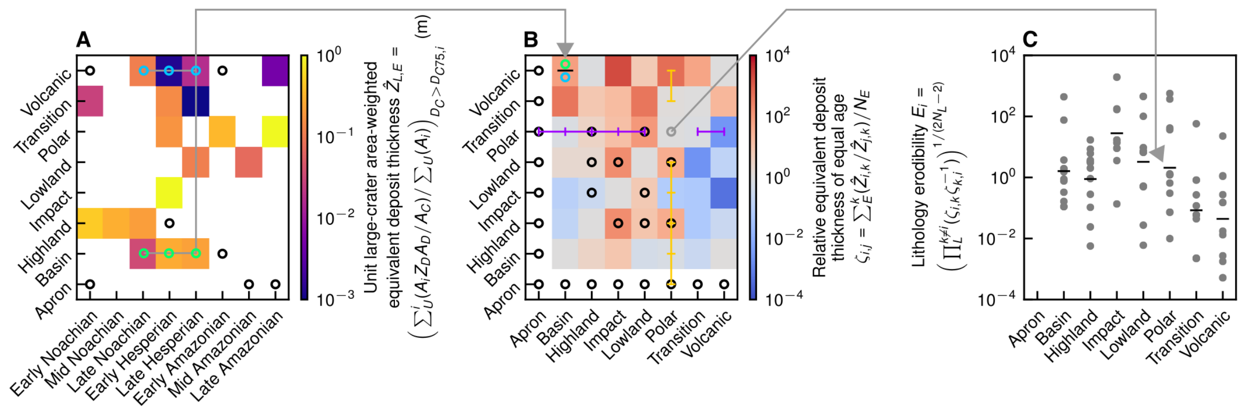

Figure S1. Illustration of relative erodibility determination. (A) The average large-crater equivalent deposit thickness weighted by unit area (defined mathematically in the colorbar label) is shown for units of given lithology (rows) and age (columns). Black dots are shown for lithology-age pairings where no craters of upper-quartile size contain eolian deposits. (B) The relative equivalent deposit thickness of lithology pairs (lithology in row over lithology in column, for a given pair) of equal age (defined mathematically in the colorbar label) is shown. Black dots are shown for lithology pairings where there are no units of equal age. (C) Lithology erodibility (defined mathematically in the y-axis label) for each lithology type; geometric mean (black lines) of all lithology comparisons (grey dots) are shown. Annotations in this figure are defined in the supplemental text.

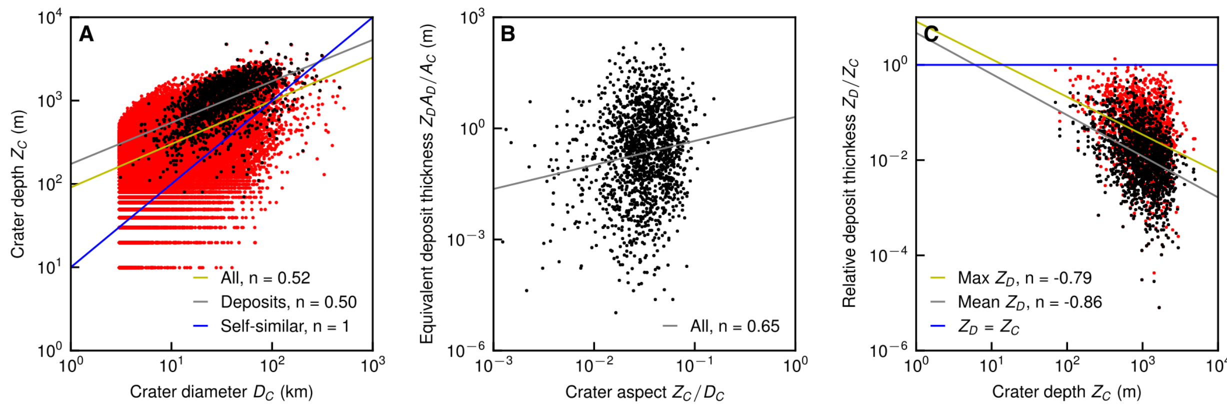

Figure S2. Extended results for crater and intracrater deposit geometries. (A) Relationship between crater diameter and crater depth (from rim to floor) as measured by Robbins & Hynek (2012) for all craters (red points) and for craters that contain eolian deposits (black points). Best-fit power laws is shown for each dataset in grey and yellow, respectively, with exponents *n* provided in the legend. If crater shapes were self-similar, the data would follow a linear relationship (blue line). The observed discretization of the data at low crater depths is an artifact arising from the fact that crater depth was only provided to the nearest 10 meter, and only for craters larger than 3 km in diameter. (B) Relationship between crater depth-to-diameter ratio and intracrater equivalent deposit thickness, with best-fit power law (grey line; exponent given in legend). (C) Relationship between crater depth and relative deposit thickness defined as the deposit thickness over the crater depth; the mean deposit thickness (black dots) and maximum deposit thickness (red dots) are both shown. Best-fit power laws are shown in grey and yellow, respectively, and the exponents *n* for these fits are given in the legend. The blue line indicates a deposit thickness equal to crater depth.

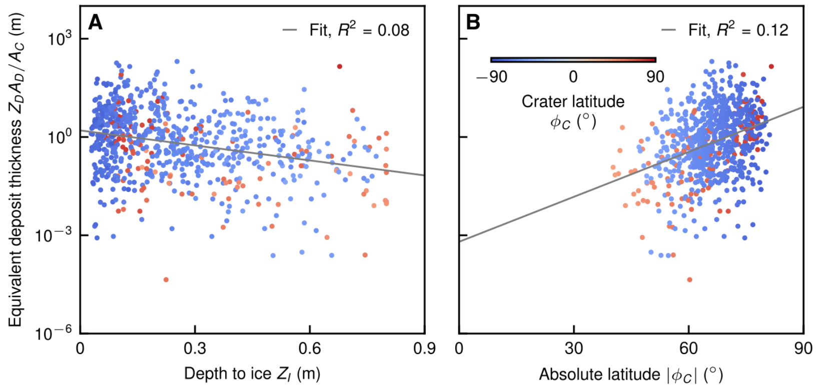

Figure S3. (A) Relationship between depth to ground ice (Piqueux et al., 2019) and eolian deposit size at high latitudes. (B) Relationship between absolute latitude and eolian deposit size. Dots are colored by latitude, best-fit power laws are shown (grey lines), and goodness-of-fit values are provided in the legend. The variance in equivalent deposit thickness is better explained by latitude than depth to ice. Note that the fit and data presented in panel B is not exhaustive; we only include data here where Z_i is defined for a direct comparison.

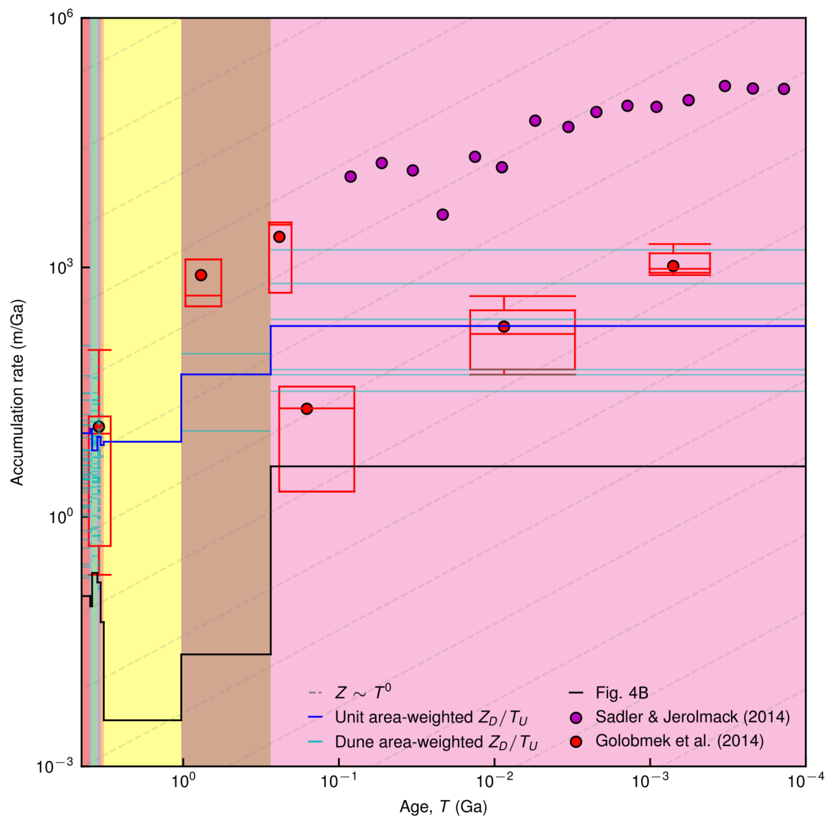

Figure S4. Comparison of our estimated accumulation rates of intracrater eolian sand on Mars to accumulation rates reported in other studies in the context of the Sadler effect. Accumulation rates are shown as a function of age on log-log axes, overlaid by shading representing Mars' geologic epochs (same legend as in Fig. 4B). Previously estimated global erosion rates on Mars (Golombek et al., 2014) are shown in red (dots = mean; box plots for median, quartiles, and ranges in rates; box width reflects age uncertainty). Purple dots represent mean aggradation rates on alluvial floodplain and continental shelves on Earth as compiled by Sadler & Jerolmack (2015) averaged over timescales shown on the x axis. Both the Golombek et al. (2014) and Sadler & Jerolmack (2015) compilations are only for non-zero thickness change systems; for a fair comparison to the intracrater eolian deposit thickness data in this study, we plot the dune-area weighted average deposit thickness accumulation rate for all units (cyan lines), and their corresponding unit-area weighted accumulation rates for each epoch (blue line). Also shown is the lithology- and spatial-bias corrected accumulation rate over time (black line) given in Figure 4B, and lines of constant deposit thickness (grey dashed lines), which would reflect the expected apparent accumulation rate bias over time for purely depositional systems (Sadler & Jerolmack, 2015).

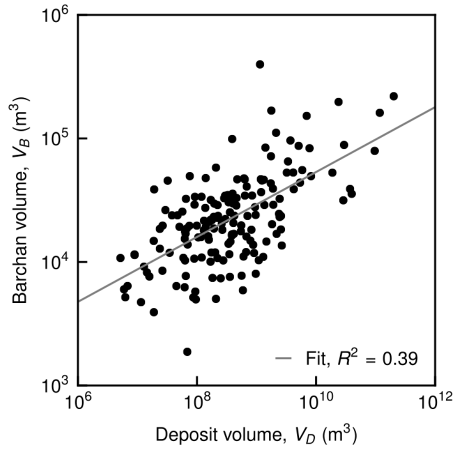

Figure S5. Comparison of MOLA-derived intracrater whole-deposit volumes with volumes of barchans in the same crater as estimated by Rubanenko et al. (in review). Sum volumes of barchans in craters where more than 30 dunes are identified are compared against our whole-deposit volumes as described in the Supplemental Materials text (N = 163). Best-fit power laws are shown (grey lines), and goodness-of-fit values are provided in the legend.